ELSEVIER

Mechanics of Materials 18 (1994) 31–48

MECHANICS OF MATERIALS

Micromechanics of stress-induced permeability anisotropy and damage in sedimentary rock

M.S. Bruno

Chevron Petroleum Technology Company, La Habra, CA 90633, USA

(Received 5 January 1993; revised version received 23 August 1993)

Abstract

A discrete element model for cemented granular material is described which combines simple mechanisms of granular deformation, intergranular and intragranular microcracking, and pore channel fluid flow. Although the microstructural mechanics are simulated with very simple and idealized models, the dominant physical processes appear to be captured with sufficient completeness that complex macroscopic behavior may be investigated, including non-linear inelastic deformation, creation and coalescence of microcracks into localized damage zones and shear bands, and stress-induced permeability alteration and anisotropy. Simulation results compare well with experimental observations, providing insight into the physical mechanisms which may control inelastic material behavior and stress-induced permeability anisotropy in weakly-cemented geological materials. The magnitude of stress-induced permeability reduction is related to the amount and strength of intergranular cementation. At low stress levels fluid permeability is reduced due to compression of intergranular flow channels. For near-hydrostatic loading permeability continues to decrease as the material compacts. At increasing deviatoric stress levels, however, compression-induced permeability reduction is counteracted by enlargement of additional flow channels due to shear and tensile damage to the intergranular bonds and compression-induced intragranular microcracking. The material yields in a dilatant manner. Because these stress-induced microcracks have preferred orientation parallel to the maximum load direction, permeability of the rock becomes anisotropic at the macroscopic level.

1. Introduction

Detrital sedimentary rock is comprised of primary grains, smaller matrix particles, pore space, and intergranular bonds resulting from cementation and overgrowths. It is the arrangement of these constituents, rather than simply their composition, which fundamentally determines the permeability of the rock – the capacity for transmitting fluid. For example, whereas porosity or clay content within some rocks of different lithology may vary by only 10% to 20%, permeability can sometimes vary by several orders of magnitude. Because individual grain contacts are non-uniform, a macroscopic stress field will produce an inhomogeneous distribution of pressures within the microstructural assembly, thereby altering the arrangement and shape of particles and pores and the permeability of the rock mate-

* *Correspondence to:* Mike Bruno, Chevron Petroleum Technology Company, P.O. Box 446, La Habra, CA 90633, USA. (E-mail: msb@chevron.com)

SSDI 0167-6636(93)E0083-E

rial. When the applied stress is anisotropic, the resulting permeability tensor may also become anisotropic.

The objective of the present work has been to investigate permeability alteration in sedimentary rock by modelling inelastic response and damage to the microstructure. A two-dimensional discrete element model is used which combines simple mechanisms of granular deformation, intergranular and intragranular microcracking, and pore channel fluid flow. The motivation for developing micromechanical models is to improve our understanding of the important and fundamental physical processes which contribute to permeability alteration and damage in rock. The goal is not simply to develop a numerical simulator capable of replicating laboratory observations. Other techniques are better suited to that task. For example, neural networks and complex constitutive models do quite well reproducing the data which were used to define their multiple parameters, but they contribute little to a fundamental understanding of physical mechanisms or microstructural characteristics which might control certain aspects of observed macroscopic material behavior. The present work attempts to address some of these questions.

A review is first presented regarding some general influences of hydrostatic and non-hydrostatic stress on permeability and damage in sedimentary rock. The microstructure of typical sedimentary rock materials is described and its control on permeability is discussed. Next, laboratory measurements of permeability changes in weakly-cemented sandstones subjected to triaxial stress are described. For these samples, stress-induced permeability reduction is demonstrated to depend strongly on the direction of applied stress, either parallel or perpendicular to flow direction. The magnitude of permeability reduction and related anisotropy is related to the initial amount and strength of cementation in the rock. Additional observations of microcrack development in sedimentary rock subject to compressive loading are also discussed.

The next two sections describe development and implementation of a discrete element microstructural model. A brief review is presented of the historical development of discrete element models for deformation in granular materials and network flow models for porous materials, followed by a description of the model used in this work. Simulation results for various biaxial loading conditions are presented. The resulting character of stress–strain curves, microfracture pattern, and permeability changes compare favorably with experimental observations, providing insight into the role played by constituent material properties and cementation in stress-induced permeability alteration and damage in sedimentary rock.

2. Stress influence on permeability in sedimentary rock

Permeability reduction due to hydrostatic stress has been investigated by many researchers, including Fatt and Davis (1952), McLatchie et al. (1958), Dobrynin (1962), Vairogs et al. (1971), Walls (1982) and Kilmer et al. (1987). Proportionately greater reduction occurs for low compared to high permeability sandstones, and also for less consolidated compared to well-cemented sandstones. For most sedimentary rocks permeability perpendicular to bedding is initially lower and generally more stress sensitive than permeability parallel to bedding.

Fabric and texture strongly influence the pressure sensitivity of sandstones. For example, many low-permeability sandstones contain high aspect ratio pores (length to thickness ratio > 100) whose flow capacity is proportionately more sensitive to stress than that of larger pores. Walls (1982) and Kilmer et al. (1987), among others, have suggested that pressure sensitivity within low permeability sandstones is more strongly influenced by pore structure than by mineral composition. When porosity and permeability is relatively high (greater than about 50 md) mineralogy can also play an important role. Both increasing clay content and decreasing cementation tend to produce a sandstone which is more compressible and pressure-sensitive. It is the structural position of the clay which most strongly influences rock properties, rather than the total abundance. Whether the clay is pore lining, pore filling, or

intragranular can have a profound effect on the resulting permeability and sensitivity to stress (Howard, 1992).

For example, consider the Kozeny–Carmen relation for permeability of porous materials (Walsh and Brace, 1984):

$$k = \phi^3 / bT^2 S^2, \quad (1)$$

where k, T, ϕ, and S are the permeability, tortuosity, porosity and specific surface area (surface area per unit volume) of the porous material. The factor b is a pore shape coefficient which ranges from 2 for circular tubes to 3 for thin cracks. Tortuosity T is the average ratio of the actual fluid path length to the apparent straight path length. For a given porosity and clay mineral content, the position of the clay influences initial permeability through its effect on tortuosity and specific surface area, while stress-induced permeability reduction will depend strongly on whether the clay supports the structural framework or is merely deposited within the pore space of a stronger grain-supported framework. When clays are primarily detrital, rather than authigenic, they will tend to support more of the microstructural framework and produce a more compliant rock.

A few researchers have studied the influence of non-hydrostatic stress on permeability, including Gray et al. (1963), Wilhelmi and Somerton (1967), Zoback and Byerlee (1976), and Morita et al. (1984). Holt (1989) investigated permeability reduction induced by triaxial stress on a relatively weak North Sea sandstone. He noted a decrease in permeability under triaxial stress when the ratio of confining pressure to axial pressure was maintained at 1:2. On the other hand, Rhett and Teufel (1992) describe permeability measurements on North Sea sandstones subjected to identical stress conditions in which permeability is initially reduced but then increases substantially at higher axial loading levels. Their tests, conducted at a variety of triaxial stress ratios, demonstrate that permeability changes in the samples tested were greatly influenced by the applied stress ratio. The importance of stress anisotropy on matrix permeability in weakly cemented sandstones are further illustrated by the experimental observations described below. Greater details regarding this work are presented in Bruno et al. (1991).

2.1. Experimental observations

Permeability measurements on three weakly-cemented sandstone lithologies were conducted under varying triaxial stress conditions up to 15 MPa. These materials are characterized by moderate to high porosity (15%–20%) and relatively high permeability (200–1000 md). The lithologies tested include Salt Wash Sandstone, Castlegate Sandstone, and Kern River Sands. A summary of the sample mineralogy is presented in Table 1.

The goal of these experiments was to compare the influence of stress applied parallel and perpendicular to flow direction on the horizontal permeability of each of the lithologies. Cylindrical rock samples, 2.5 cm in diameter and 7.5 cm in length, were cut parallel to bedding and loaded into a standard triaxial cell. Computer controlled hydraulic pumps were used to independently control and maintain radial and axial pressure loading on the rock samples. The core samples were surrounded by a heat-shrinkable teflon sleeve to separate the confining pressure from pore fluid pressure. A third computer controlled pump was used to flow a low viscosity oil through the samples at precise flow rates, ranging from 1.0 to 4.0 cc/min, with an accuracy of about 0.01 cc/min. A high-precision quartz transducer was used to measure the pressure drop along the length of the rock samples.

Table 1
Rock sample texture and mineralogy

	Salt Wash	Castle-gate	Kern River
Quartz grains (%)	35	56	12
Feldspar grains (%)	5	5	18
Lithic fragments (%)	22	8	30
Authigenic clays (%)	8	4	10
Silica cement (%)	0	1	0
Calcite cement (%)	5	0	0
Grain size (μm)	250–500	65–125	250–500
Sorting quality	very well	well	poor
Oil permeability (md)	600–800	850–950	300–500
Porosity (%)	25	26	30

The samples were first loaded hydrostatically to a pressure of about 3 MPa, and an initial permeability was measured. To assess the influence of load applied parallel to the flow direction, only the axial load was increased and permeability measured at increments of about 3 MPa up to about 12 to 15 MPa. Permeability was also measured as the axial load was decreased back to the initial hydrostatic conditions. To assess the influence of load applied perpendicular to the flow direction, the radial load was next increased. Permeability was measured at increments of about 3 MPa up to about 12 to 15 MPa, and again as the radial pressure was unloaded. Figs. 1, 2, and 3 present examples of the stress-induced permeability reduction for typical Salt Wash, Kern River, and Castlegate samples, respectively. In Figs. 1 and 2 the reduced permeability is expressed as a percentage of the initial permeability at the start of the loading cycle.

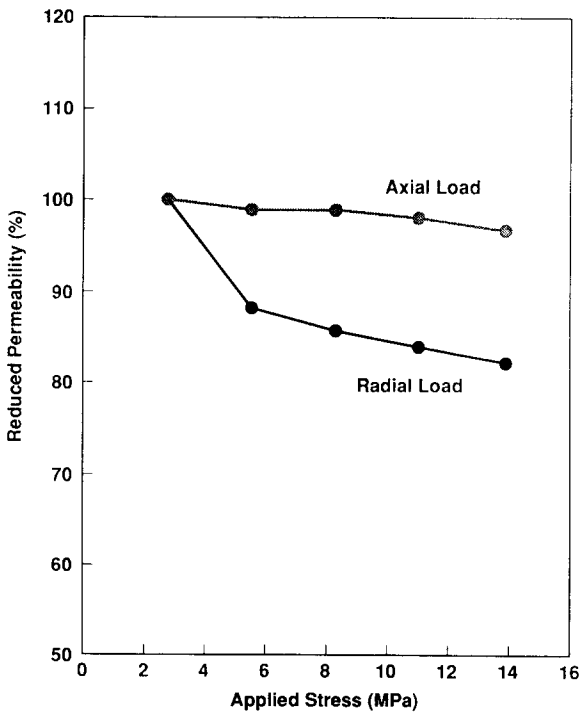

Fig. 1. Typical permeability reduction for Salt Wash sample. Permeability at increased stress is expressed as a percentage of permeability at initial stress.

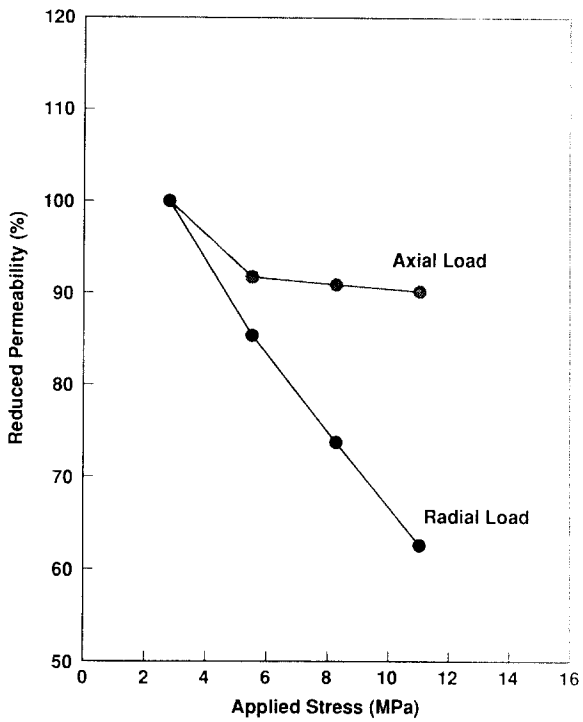

Fig. 2. Typical permeability reduction for Kern River sample. Permeability at increased stress is expressed as a percentage of permeability at initial stress.

The permeability of each sample was reduced only slightly when subjected to loading parallel to the flow direction. When loaded perpendicular to the flow direction (radial load), the permeability of each sample was more significantly reduced. Note that a larger reduction in permeability is produced by the radial load cycle, even though some irreversible permeability damage remains from the initial axial load cycle. Fig. 3 illustrates the typical permanent reduction in permeability for the Castlegate sample, showing the complete loading and unloading cycles for both axial and radial stress. Similar results were obtained when the order of loading was reversed. That is, under the radial load cycle significant permeability reduction occurs, while under the axial load cycle almost no further reduction takes place. Some of the mechanisms which might contribute to this stress-induced permeability anisotropy are described in Section 3.

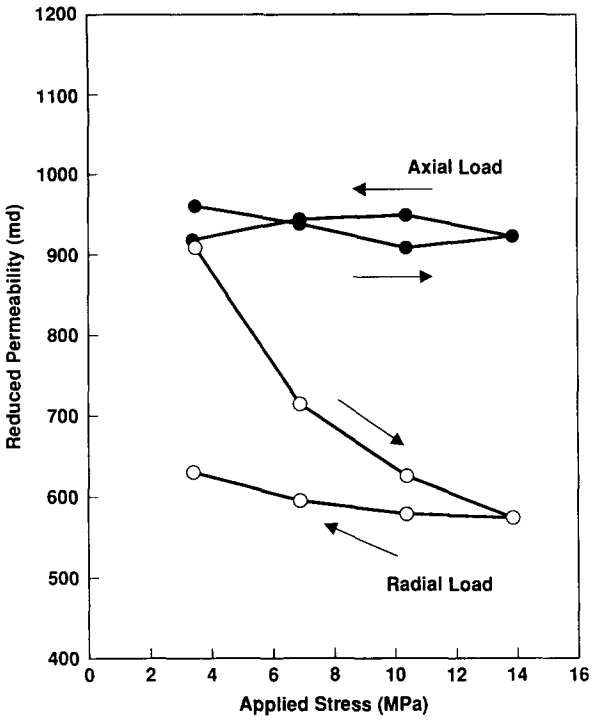

Fig. 3. Complete load–permeability curve for Castlegate sample.

The significant permanent reduction in permeability demonstrated by Fig. 3 suggests that irreversible compaction and deformation is the primary mechanism for permeability alteration. There was a general trend towards increased stress sensitivity with decreasing amount and strength of cementation. Among the lithologies tested, the Salt Wash samples were most strongly cemented, with about 5% calcite. Next in cementation strength were the Castlegate samples, whose grains were more weakly bonded by pore bridging clay and trace amounts of silica cement. The Kern River samples, which were almost completely unconsolidated, were most sensitive to stress.

3. Stress-induced microcracking and damage

What mechanisms are responsible for the difference in permeability reduction caused by stress applied parallel to flow compared to permeability reduction caused by stress applied perpendicular to flow? The pattern and orientation of stress-induced microfracturing in rocks provides a possible explanation. As compressive stress is first applied to a sample, microfractures occur at grain boundaries and are predominantly oriented parallel to the primary loading axis (Peng and Johnson, 1972; Zheng et al., 1989). The microcracks are inititally distributed uniformly throughout the sample and later coalesce and concentrate in narrow deformation bands (Hoshino and Koide, 1970; Hallbauer et al. 1973; Lockner et al. 1992).

At higher stress levels, axial cracks are lengthened to a greater extent than cracks with different orientations Bombolakis, 1973). In addition, intragranular microcracks develop, again oriented predominantly in the axial direction (Tapponnier and Brace, 1976; and Hallbauer et al., 1973). These are most often extension type microcracks initiated at grain contact points. The process is similar to that which occurs during Brazilian tests when circular disks are compressed between point loads, producing a central region of uniform tensile stress. Gallagher et al. (1974) have illustrated this internal fracture pattern in sandstone disks, glass beads, and quartz grains. Within sedimentary rock, grain boundary cracking (or grain slippage and rotation) occurs more frequently than intragranular fracture. This is especially true for uniaxial or low confining pressure stress conditions (Sangha et al., 1974) but will also occur during the initial stages of hydrostatic compression loading (Zhang et al., 1990).

Because triaxial stress produces microcracking and damage within the microstructure of sedimentary rock, at least three mechanisms for permeability alteration may be identified. The first mechanism simply involves pore volume compressibility and associated permeability reduction, due to reduction in average pore throat radii. A second and closely related mechanism is the preferential closure of existing microcracks and high aspect ratio pores which are oriented more perpendicular to the direction of maximum stress. A final mechanism is the creation of additional flow channels due to shear and tensile damage to the intergranular bonds and compression-induced intragranular microcracking.

Since fluid flow through shear cracks under compression is not expected to change considerably with increased deformation, the tensile cracking at grain boundaries and within grains will dominate changes in fluid flow capacity. Because the tension microcracks are oriented predominantly parallel to the direction of maximum stress, permeability in this direction increases. At high deviatoric stress conditions permeability increase caused by dilating stress-induced microcracks and oriented high aspect ratio pores may completely counteract the compaction-induced permeability reduction. These potential mechanisms for stress-induced permeability anisotropy are investigated with the micromechanical model described in the next few sections.

4. Micromechanical model development

4.1. Granular deformation models

In this work a discrete element model is applied to investigate deformation and permeability behavior of cemented granular materials. Numerical simulation of cohesionless granular assemblies with discrete elements was introduced by Cundall and Strack (1979), and has since been applied to investigate constitutive relations and stress-induced fabric anisotropy for granular materials (Bathurst, 1985; Rothenburg and Bathurst, 1989). In these models, the movements of circular discs and contact forces are tracked with an explicit finite difference procedure. Particle interaction is modelled by damped force–displacement relations at each disc contact and the resulting forces and moments are related through Newton's second law to the particle mass and acceleration. The dynamic system can approximate static equilibrium conditions when sufficient contact and global damping is added and loading rates are kept low. Contact forces on the microstructural level may be related to macroscopic boundary stresses through the principal of virtual work (Christofferson et al., 1981; Oda et al., 1982; Mehrabadi et al., 1982; Bathurst and Rothenburg, 1990).

Relatively fewer researchers have applied discrete element models to investigate cemented granular material behavior. Plesha and Aifantis (1983) described a model for polygon shaped particles sharing straight boundaries in which elements are defined at each interface to resist normal and shear deformation. They used the model to investigate compression-induced crack development in rock. Zubelewicz and Bazant (1987) applied an interface element model to study tensile fracture in aggregate composites such as concrete.

Bruno and Nelson (1991) applied a similar model to study microfracturing in porous sedimentary rock under biaxial load conditions. This model included the additional capability to simulate intergranular shear fracture and compression-induced grain fracture. In modelling granular materials with cohesion, frictional contact interaction is replaced with force–displacement behavior of a deformable interface element, representing the intergranular bonding of cementation and overgrowths. The interfaces and force interaction with neighboring particles do not lie on a circle of constant diameter but on a polygon of irregular shape. Because all grains are assumed to be bonded to at least one neighbor, static equilibrium is continuously maintained and a dynamic solution procedure is not required. The model may also be applied to investigate permeability changes by adding a pore space flow network.

4.2. Network flow models

Since the pioneering work of Fatt (1956a–c), network models have been used extensively to study fluid transport in porous media (Chatzis and Dullien, 1977; Dullien, 1979; Rothenburg et al., 1987). In porous media fluid flows through systems of interconnected conduits of varying shape and size. For single phase fluids, simple network theory is based on the analogy between Darcy's law for fluid flow and Ohm's law for current flow. That is, the flow rate is proportional to the conduit permeability (conductivity) and the difference in pressure (voltage) between the endpoints. In fact the earliest flow models were built

with networks of variable size resistors as analog computers (Fatt, 1956; Probine, 1958). Modern digital computers now allow the analysis of large scale two- and three-dimensional networks to study transient and steady-state multi-phase flow problems.

More recently, a few researchers have combined network flow models with mechanical deformation models for porous materials. Seeburger and Nur (1984) developed a two-dimensional network model to investigate changes in permeability and bulk modulus as a function of hydrostatic confining pressure. They applied Hagen–Poiseuille type expressions for flow through elliptic and tapered conduits with pressure dependent cross sectional areas. The effective bulk modulus varied with pressure according to cracked solid models described by Walsh (1965) and Mavko and Nur (1978). Yale (1984) developed a three-dimensional model to simultaneously study permeability, electrical conductivity (formation factor), and porosity at varying hydrostatic pressure conditions. He investigated the influences of various pore shapes and pore sizes on the physical properties of rocks and the ways in which the properties were interrelated. Thallak et al. (1991) developed a flow-coupled discrete element model and applied this towards the investigation of hydraulic fracture (parting) in cohesionless granular assemblies. They employed the distinct element model for dynamic granular deformation developed by Cundall and Strack (1979) and added a channel flow network defined by the space between particles. Fluid flow was modelled by the Hagen–Poiseuille equation for circular conduits. Body forces acting on the particles due to fluid flow were calculated by integrating the pore pressure over individual grain boundaries.

4.3. Damage and flow model for sedimentary rock

The model used in this work to simulate stress-induced damage and permeability alteration is a modified version of the 2-D discrete element model for sedimentary rock developed by Bruno and Nelson (1991) with the addition of a deforming fluid flow network (Fig. 4). A brief summary of the mechanical deformation aspects of the model is provided below, followed by a description of the fluid flow network.

4.3.1. Mechanical deformation

Intergranular bond elements are defined by regions of overlapping cementation and overgrowth layers around individual grains as shown in Fig. 5. The element width, W, is defined by the extent of layer overlap and the element length, L, is defined by the separation distance between grain surfaces. As the grain centers rotate and translate, the bond elements resist normal and shear deformations through simple force displacement relations.

$$\begin{Bmatrix} f_n \\ f_s \end{Bmatrix} = \begin{bmatrix} K_n & 0 \\ 0 & K_s \end{bmatrix} \begin{Bmatrix} d_n \\ d_s \end{Bmatrix}, \tag{2}$$

where $K_n = EW/L$ and $K_s = GW/L$. The variables f_n and f_s represent the element restoring forces acting on the grains. The stiffness coefficients K_n and K_s are proportional to the initial bond width and inversely proportional to the initial bond length. E and G represent normal and shear stiffness factors for the bond material, similar to the Young's and shear moduli. Although the interface elements define an interior body of irregular shape, the grain cross sections are assumed to be sufficiently circular that element forces act on a common center. Some limitations of this assumption are discussed by Bruno and Nelson (1991). The normal and shear forces of several bonds acting on a particular grain are resolved into a single force vector (two force directions and a moment) at the grain center with components F_x, F_y, and F_θ. The deformation variables d_n and d_s for each bond are uniquely determined by the displacement components u_x, u_y, and u_θ of the grain centers attached to each side of the bond.

The intergranular bonds are assumed to deform in a linear elastic manner within limits defined by a bi-linear failure envelope shown in Fig. 6. The uniaxial tensile strength of the bonds are defined by point C_t on the horizontal axis. The limit under pure shear loading is defined by point C_s on the vertical axis. Tensile failure is modelled as completely brittle, resulting in total loss of

normal and shear stiffness. This is accomplished by setting the normal and shear stiffness coefficients, K_n and K_s, for that particular bond to 0.001 times the initial values for all additional loading of the microstructure assembly. When loading on an individual bond exceeds the shear limit, the shear stiffness of the material is reduced significantly (from 50% to 90%). The normal stiffness is eliminated for additional tensile displacement but remains unchanged for additional compressive displacement.

Individual grains may also become damaged due to compressive point loading in the manner demonstrated by Gallagher et al. (1974). Grain fracture is assumed to occur when the following criterion is satisfied,

$$\frac{f_n}{\pi r_g} \geq C_g, \tag{3}$$

where f_n is the maximum normal load from any bond attached to the grain, r_g is the grain radius, and C_g is the grain material tensile strength. Internal grain fracture is assumed to shatter the grain sufficiently that all connecting bonds with neighboring grains are broken and the associated normal and shear stiffness contributions are eliminated.

4.3.2. Fluid flow network

Fluid in the model is defined to flow through a network of deformable pore space conduits. There are obvious difficulties in attempting to model three-dimensional tortuosity with a two-dimensional network, but a few simplifying assumptions may be qualitatively reasonable. Within the plane of the 2-D grain assembly cross section, pore conduit connections are located at the centroid of interconnected cementation bonds (Fig. 4). It is assumed that the cross sectional area and flow capacity of the pore space conduits are controlled by the deforming bond between the conduit endpoints. At first glance this may seem counterintuitive – within the plane the cementation bonds appear to block fluid flow. In three dimensions, however, the pore space connecting two intergranular points actually wraps around the bond separating those points. The 2-D grain assembly

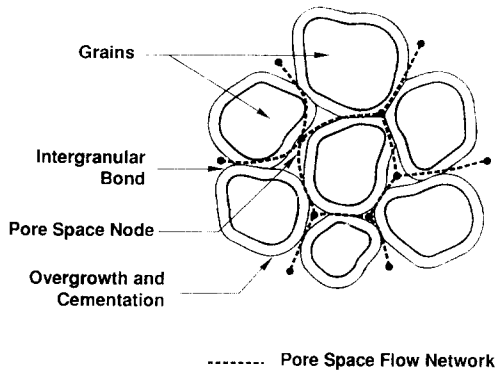

Fig. 4. Discrete element microstructure model.

can be thought of as not infinitely thin, but rather of finite thickness containing the grain layer and one layer of pore space out of the plane. If we assume that for two-dimensional deformation and flow the behavior of the chosen cross section is similar to that of parallel layers above and below, the shape of the pore space conduits which wrap above and below the bond between two grains is controlled by the deformations of that bond. As a first approximation, the conduit shapes are assumed to be roughly circular with minimum radii r_p proportional to the grain separation distance (bond length L) and with path lengths l_p proportional to the amount of cementation overlap (bond width W).

The radii of the conduits deform with applied load, resulting in non-constant flow network properties. Bond fracture acts to reduce the intergranular stiffness and hence makes conduit sizes even more deformable with additional loading. Grain fracture is accommodated by coalescing the surrounding pore space conduits into a single larger conduit. Flow rate Q is assumed to be proportional to the pressure difference between the endpoints ΔP and to the fourth power of the conduit radius, and is inversely proportional to the conduit path length, consistent with Hagen–Poiseuille pipe flow:

$$Q \propto \frac{r_p^4}{l_p} \Delta P. \tag{4}$$

The initial geometrical form of the pore space network described here is similar to the channel

network for cohesionless granular assemblies applied by Thallak et al. (1991). The significant difference between the two flow models is that the network elements used in this work have stress-dependent geometry and transport properties.

4.3.3. Solution procedure

The grain model is assembled by placing grains of varying diameters (from 0.4 to 0.6 mm) at random locations within a 1.0 cm × 2.0 cm area representing the sample cross section until a specified areal density is achieved (usually about 60%). The grains need not be touching, but are not allowed to overlap. Next a layer of cementation and overgrowths is added to each grain with a thickness proportional to the individual grain diameters. The grain size distribution and amount of cementation and overgrowth may be varied to simulate different petrographic properties.

Element force–displacement relations are defined by the amount of granular cementatation and overgrowth. The element equations for the assembly of grains are combined to form a set of system equilibrium equations of the form,

$$\{F\} = [TM]^{\mathrm{T}}[KM][TM]\{u\}, \tag{5}$$

where $\{F\}$ represents the column vector of grain center force components, $[TM]$ is a geometric tranformation matrix relating element deformation and forces to global displacements and forces (Bruno and Nelson, 1991), $[KM]$ is the diagonal matrix of bond element stiffnesses, and $\{u\}$ is the column vector of grain center displacements.

A system of flow equations for the pore space network can be expressed in a similar form,

$$\{Q\} = [A][KP][A]^{\mathrm{T}}\{P\}, \tag{6}$$

where $\{Q\}$ is the column vector for the volume flow rate from an external source applied at each node, $[KP]$ is the diagonal matrix of hydraulic conductivities of the pore space conduits (Eq. (4)), and $\{P\}$ is the fluid pressure at each node. $[A]$ is an incidence matrix defined such that $A_{ij} = 1$ when the flow in conduit j is directed into node i; $A_{ij} = -1$ when the flow in conduit j is directed away from node i; and $A_{ij} = 0$ when conduit j does not flow into node i.

The final system Eqs. (5) and (6) are easily solved for constant stiffness and conductance coefficients. As individual bonds and grains break, stiffness and conductance terms must be modified. The cumulative system response is obtained with the following step-by-step procedure:

(1) Assemble the system equations for deformation and flow based on the initial geometry and connectivity of the bonded grains.

(2) Apply a small amount of boundary flow to the network model and solve Eq. (6) for the initial pore pressure distribution and steady-state permeability.

(3) Apply a unit increment of force, representing boundary loads, and solve Eq. (5) for the grain center displacements, u.

(4) Evaluate the resulting bond deformations and forces thoughout the body. Determine the load factor required to induce the next bond or grain fracture and the failure location. Record the resulting macroscopic load and displacement.

(5) Modify the global stiffness matrix by reducing the contribution of failed elements. Re-assemble the global conductance matrix, taking into account deformed conduit sizes and changes in connectivity due to deformation and grain fracture.

(6) Return to step (2) and repeat the process, continuing to monitor fracture development, load, deformation, and permeability changes.

Boundary flow rates and resulting pore pressures are defined arbitrarily small, so that the influence of pressure gradients (body forces) on deformation may be considered negligible compared to mechanical loading effects and no direct coupling is required. Steady-state permeability is determined at time scales much larger than the loading rate, so that transient fluid flow effects may also be neglected.

At the start of each incremental load step all of the grain particles are rigidly connected (although some of the connections have nearly zero stiffness due to past tensile failure). The equilibrium Eqs. (5) and (6) are uncoupled and do not include velocity or acceleration terms. This greatly simplifies the solution procedure. The static equilibrium equations may be solved directly without the need for global damping or dynamic solution

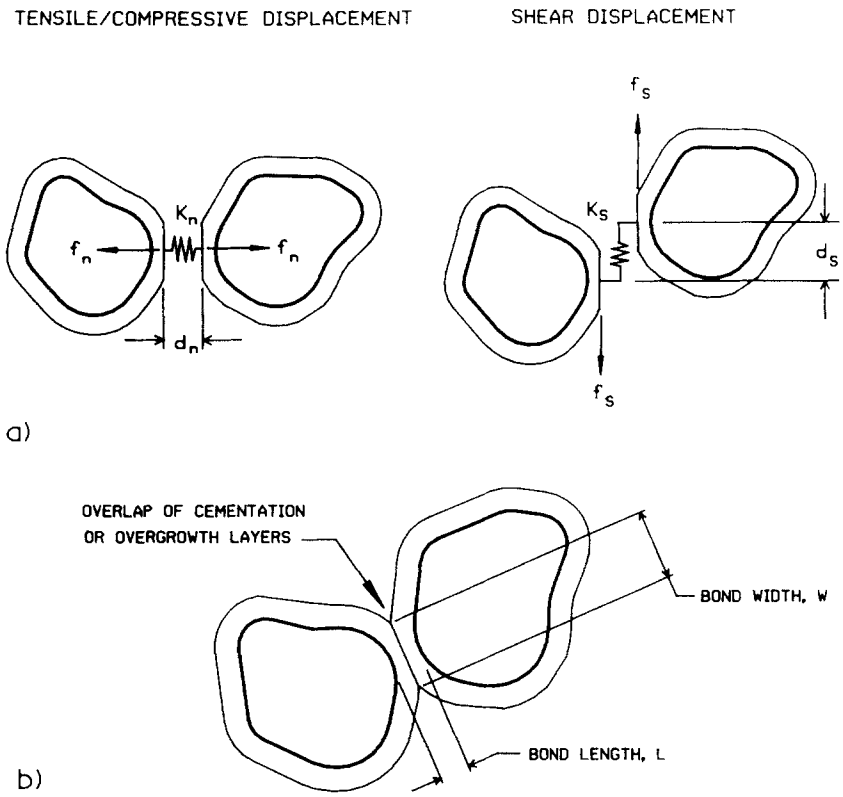

Fig. 5. Bond element force–displacement relations.

methods. This is in contrast to the dynamic procedure employed by Cundall and Strack (1979) for cohesionless granular assemblies of discrete particles with velocities, accelerations, and inertia. The solution algorithm employed in this work is the International Math and Statistics Library routine LSAQS, which uses a variation of the Gause elimination procedure with Cholesky factorization and iterative refinement (IMSL, 1987).

5. Simulaton results

Several models with up to 1500 grains and 3000 pore space conduits have been simulated to investigate stress-induced damage and permeability change in sedimentary rock. The model shown in Fig. 7 is comprised of 1100 grains with diameters ranging from 0.4 to 0.6 mm. The area grain density is 64%. The amount of cementation and overgrowth ranges from 0.10 to 0.15 mm resulting in an average number of intergranular bonds per grain (coordination number) of 4.9. The associ-

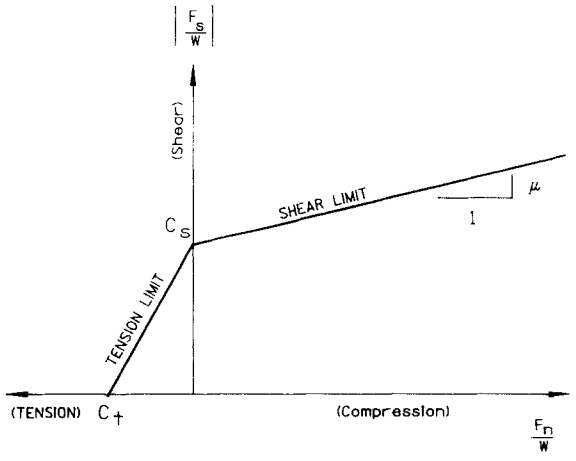

Fig. 6. Intergranular bond failure criteria.

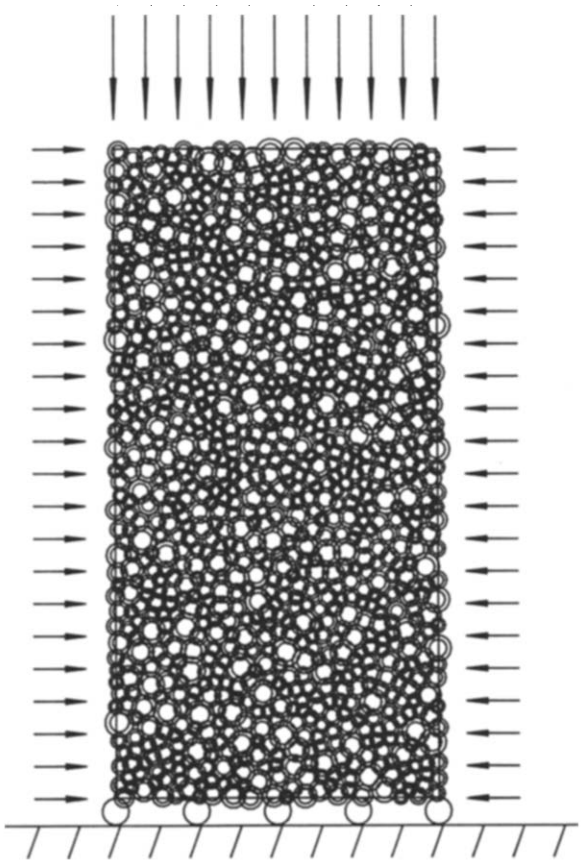

Fig. 7. 1100 grain model subject to biaxial compression.

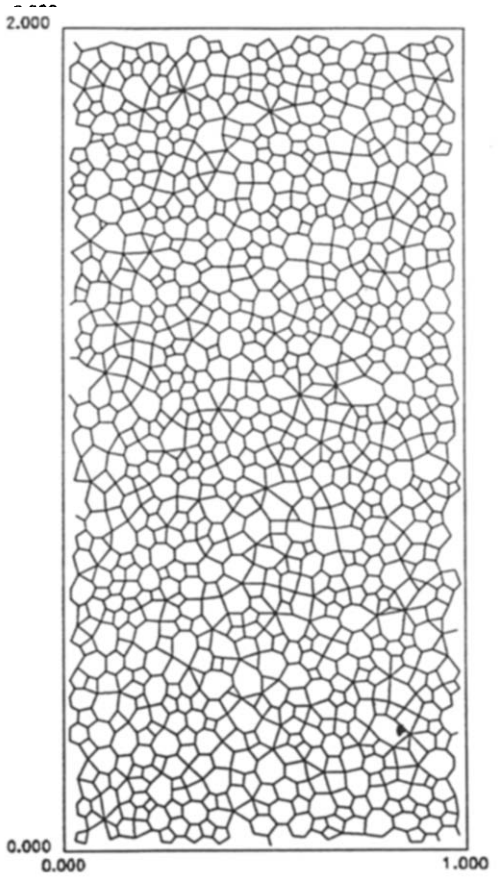

Fig. 8. Pore space network flow model.

ated pore space network model is shown in Fig. 8. Material properties for the system elements are summarized in Table 2.

5.1. Biaxial load behavior

In the first set of simulations a biaxial load is applied to the grain assembly with an axial to lateral load ratio of 4:1, as shown in Fig. 7. The flow rate into the bottom of the model is balanced with flow out of the top. No flow occurs out of the sides. Fig. 9 presents the resulting load, permeability, and microcrack behavior and their interactions. In Fig. 9a the axial load normalized with respect to peak load and the single phase steady-state permeability normalized with respect to initial permeability are plotted against axial strain. In Fig. 9b the frequency of microcrack occurrences are also plotted against axial strain. The general character of each of these curves matches typical experimental observations on sedimentary rock deformation (see for example, Paterson, 1978).

The onset of microstructural damage, as evidenced by microcracking and a break in the linear behavior of the load-deformation curve, occurs at about 60% of the peak ultimate load level.

Table 2
Material property factors used in biaxial load example (quantities are dimensionless)

Normal stiffness factor, E	200
Shear stiffness factor, G	400
Bond tensile strength, C_t	10
Bond shear strength, C_s	20
Grain tensile strength, C_g	80

This is also the approximate point at which the stress-induced permeability reduction begins to flatten. The microcrack pattern at 75% of peak load (point A) is illustrated in Fig. 10a. At this time microcracks are distributed somewhat randomly throughout the sample, with the most dominant orientation in the direction of maximum stress (axial). Just before and when peak load is reached, a sharp increase in permeability and microcracking begins. This behavior accelerates during the steep unloading portion of the curve as microcracks coalesce into a macroscopic shear failure pattern. This macroscopic failure pattern becomes evident at peak load (point B) and with

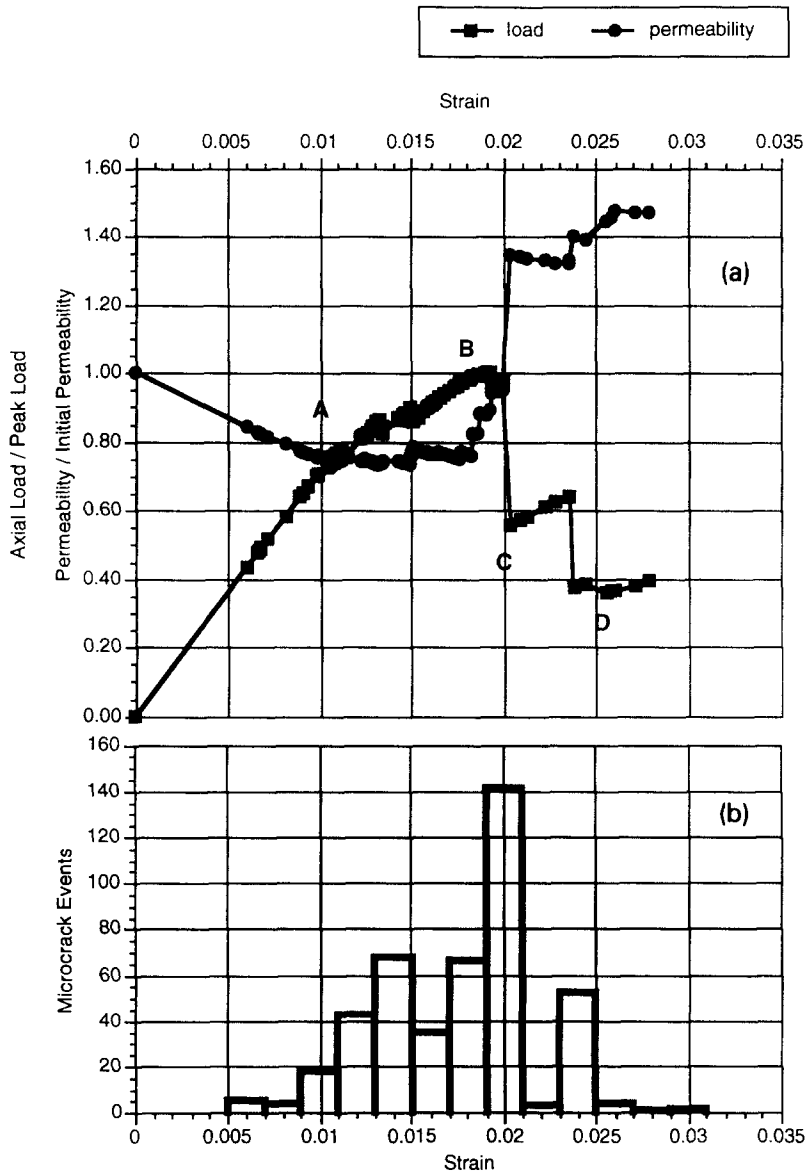

Fig. 9. Permeability, load, and microcrack events vs. axial strain for model subject to biaxial compression (axial-radial load ratio is 4:1): (a) permeability is normalized with respect to initial permeability and load is normalized with respect to peak load; (b) presents total number of microcracks occurring over specified strain interval.

subsequent loss in load bearing capacity (point C). The greatest amount of microcrack activity and permeability increase actually takes place during the unloading portion of the curve. During this stage microcracks coalesce into a localized shear band (damage zone) inclined at an angle to the maximum load direction, as shown in Fig. 11. The orientation of stress-induced microcracks is presented in Fig. 12 and compared with the initial isotropic orientation of all interfaces. The induced microcrack orientation is anisotropic, with the greater number oriented more parallel to the load direction.

5.2. Cementation influence on permeability reduction

Because damage in sedimentary rock primarily occurs at grain boundaries, it is the properties of the grain bonds which most strongly control permeability reduction. To illustrate this point, several simulations were performed with varying cementation amounts and stiffness characteristics. Fig. 13 presents results for the biaxial loading case described earlier and compares permeability reduction for varying bond stiffness ratios. Although the general permeability behavior for each case is similar, a 40% reduction in bond stiffness from the properties described in Table 2 nearly doubles the relative permeability reduction. For each case the bond failure properties were held constant. These simulations are qualitatively consistent with experimental data comparing permeability reduction for lithologies with increasing amounts of cementation, presented in Fig. 14. Bernabe et al. (1992) have demonstrated that relatively minor amounts of cementation deposited at grain boundaries can significantly strengthen granular rocks.

Although the microstructural model described in this work is simple, a variety of material characteristics for different lithologies may be investigated. The behavior of weakly cemented and compliant materials, for example, may be captured with reduced bond stiffness properties. The degree of cohesion between grains may be con-

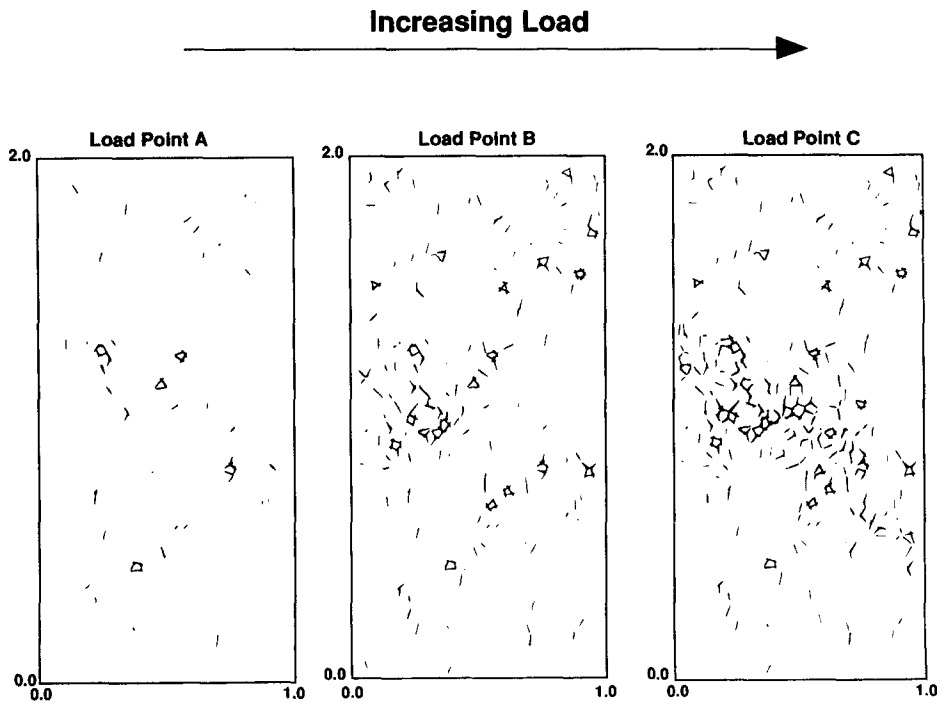

Fig. 10. Development of microcracks at various load levels for biaxial compression simulation. (Points on load curve illustrated in Fig. 9.)

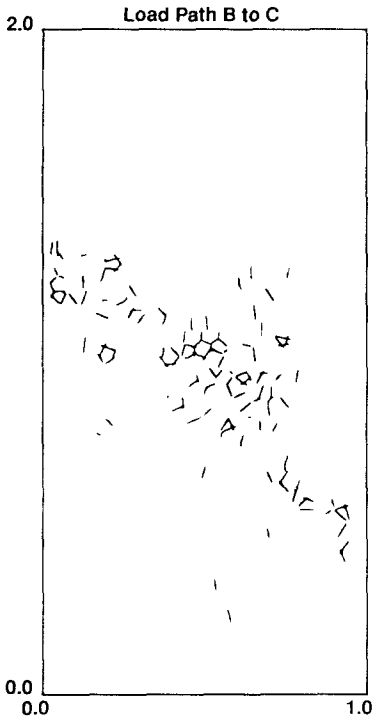

Fig. 11. Microcrack concentration into macroscopic shear band during unloading portion of load–deformation curve (point B to C, Fig. 9).

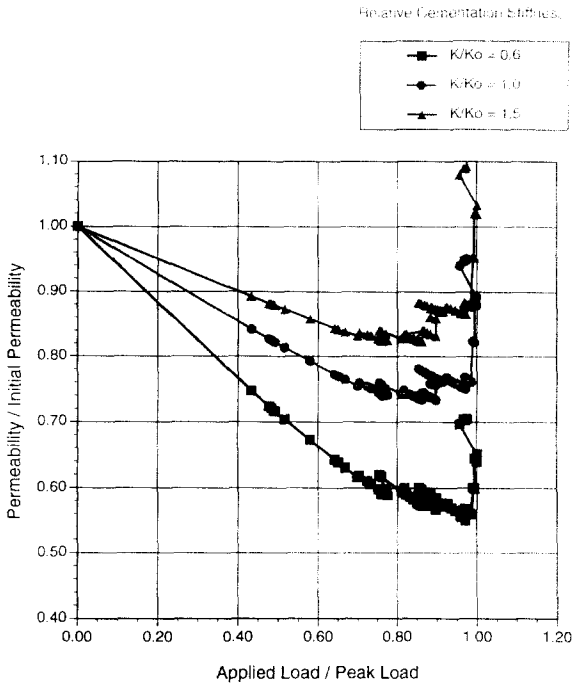

Fig. 13. Permeability reduction is sensitive to intergranular bond stiffness. Stiffness ratios (K/K_0) refer to scale factor applied to elastic properties given in Table 2.

trolled with the bond tensile strength parameter C_t. The degree of grain interlocking (for example sutured vs. point contact) may be controlled with the shear stiffness and strength parameter, C_s. The inherent grain strength may be controlled with the grain tensile strength C_g.

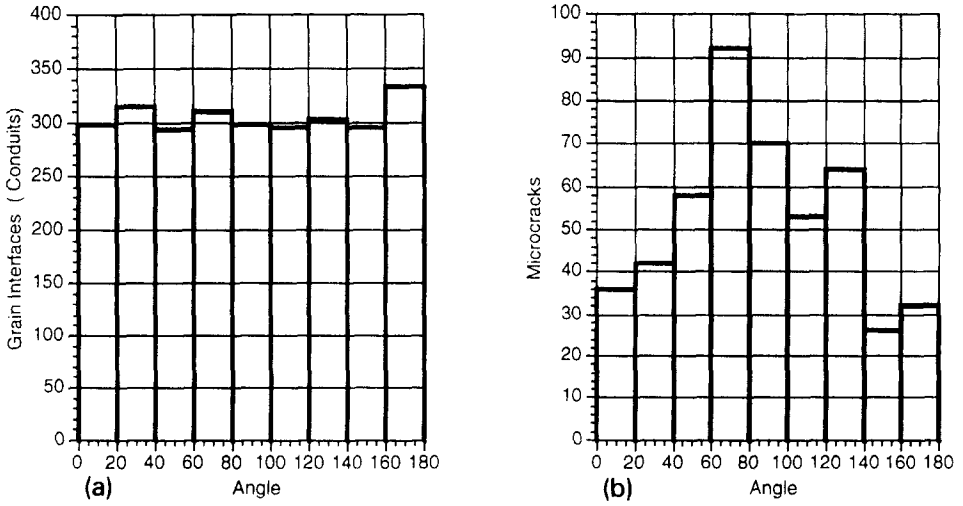

Fig. 12. (a) Orientation of all interfaces is isotropic; (b) orientation of stress-induced microfractures is anisotropic with most aligned more parallel to maximum load direction (90°).

5.3. Stress direction influence on permeability reduction

To investigate the influence of stress direction on permeability reduction in weakly cemented sandstones, simulations were conducted under uniaxial loading conditions, both parallel and perpendicular to flow. The results of one such comparison is presented in Fig. 15, for the material properties given in Table 3. Permeability reduction with respect to initial permeability is plotted vs. load, normalized with respect to peak load. At the highest load levels, the reduction in permeability due to stress applied perpendicular to flow direction is more than four times the reduction due to stress applied parallel to flow direction. The general character of these results compares favorably with the experimental observations described earlier and illustrated in Figs. 1–3.

The behavior of the microstructure controls the differences in stress-induced permeability reduction for load applied parallel and perpendicular to flow. Permeability is influenced more strongly by flow channels oriented parallel to the flow direction. The widths (and transport properties) of these channels are influenced more strongly by load applied perpendicular to their orientation. The result is that a non-hydrostatic stress field induces permeability anisotropy by preferential closure of pore space conduits aligned more perpendicular to the direction of maximum stress. This effect would be enhanced for lithologies with high aspect ratio pores, such as the tight gas sands which have been experimentally observed to be highly stress sensitive (Vairogs et al., 1971; Kilmer et al., 1987).

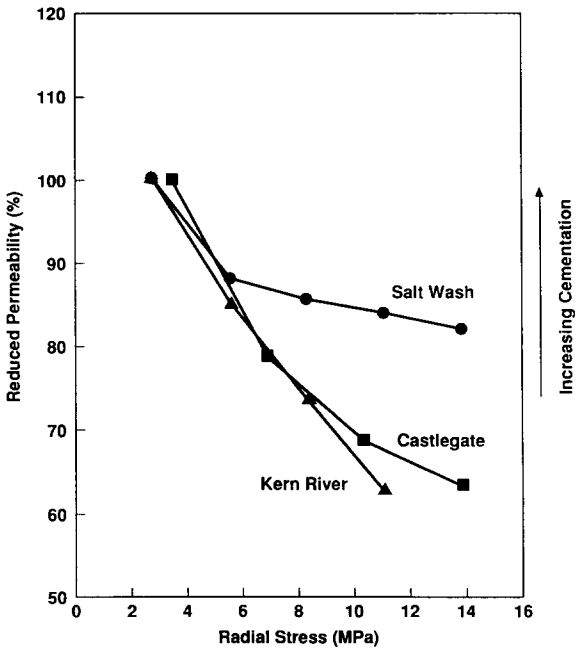

Fig. 14. Stress induced permeability reduction is controlled qualitatively by cementation strength in samples tested.

Table 3
Material property factors used in uniaxial load examples (quantities are dimensionless)

Normal stiffness factor, E	120
Shear stiffness factor, G	120
Bond tensile strength, C_t	5
Bond shear strength, C_s	20
Grain tensile strength, C_g	80

In addition to preferential closure of existing microcracks and high aspect ratio pore space conduits, an anisotropic stress field also modifies permeability through crack extension and creation of new microcracks. To illustrate this point, consider the orientation of stress-induced microcracks shown in Figs. 16a and 16b for the axial and radial load simulation presented earlier (Fig. 15, Table 3). The orientations of induced microfractures are dominantly aligned parallel to the direction of maximum stress, consistent with the experimental observations discussed in Section 3. Such preferred orientation of induced microcracking was also seen in the biaxial stress simulation (Fig. 12).

6. Conclusions

A discrete element model for cemented granular material which combines simple mechanisms of granular deformation, intergranular and intragranular microcracking, and pore channel fluid flow has been applied to investigate stress-induced permeability alteration and damage in sedimentary rock. It has been demonstrated that with very simple and idealized models the dominant physical processes at the microctructural level may be captured with sufficient complete-

ness that complex macroscopic behavior can be simulated, including non-linear inelastic deformation, dilation and compaction, creation and coalescence of microcracks into localized damage zones and shear bands, and stress-induced permeability alteration and anisotropy.

Simulation results compare well with experimental observations. Microcracking, non-linear deformation, and a decrease in the rate of permeability reduction commences at between 60% to 80% of peak load level. An increase in microcracking activity occurs very near peak load and immediately during the subsequent unloading phase, consistent with typical acoustic emmisions observations. This is the same period during which permeability parallel to the load direction increases substantially for dilating rock, providing an indication of microstructural damage. The laboratory experiments described in this work did not attempt to capture significant permeability increases during axial failure, because the test procedure required controlled unloading of axial pressure prior to failure and subsequent increase in radial pressure (Fig. 3) in order to compare relative influences of stress direction. However, previous experimental work by several researchers, including Mordecai and Morris (1971) and Lee and Juang (1988), have clearly demonstrated such an increase in permeability at axial failure in sandstones, and the coincidence of the permeability increase with the onset of significantly increased acoustic emissions have been demonstrated in many triaxial tests on granite (see for example, Paterson, 1978).

The magnitude of stress-induced permeability reduction is related to the amount and strength of intergranular cementation. At low stress levels fluid permeability is reduced due to compression

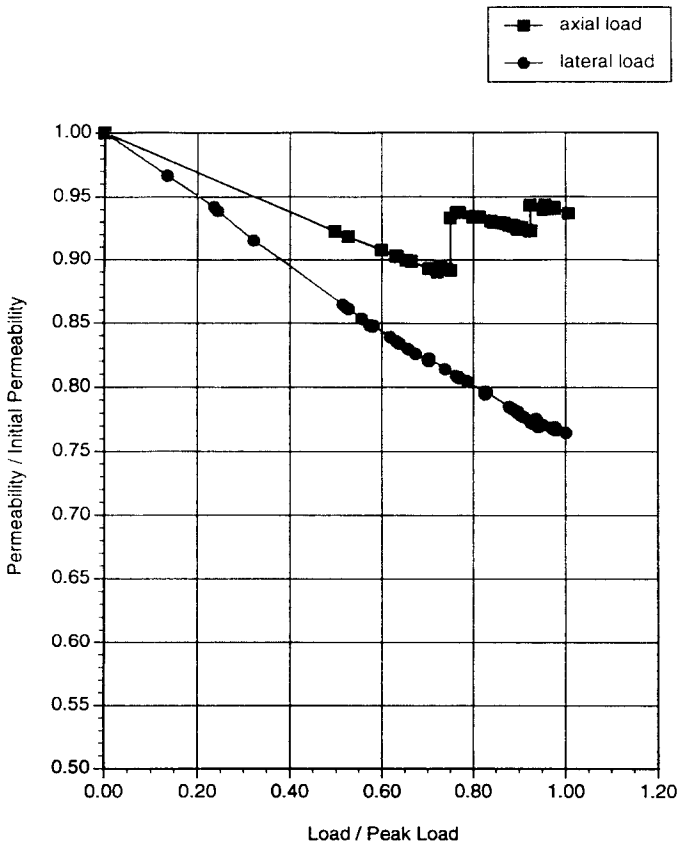

Fig. 15. Axial permeability reduction induced by radial load is greater than that induced by axial load.

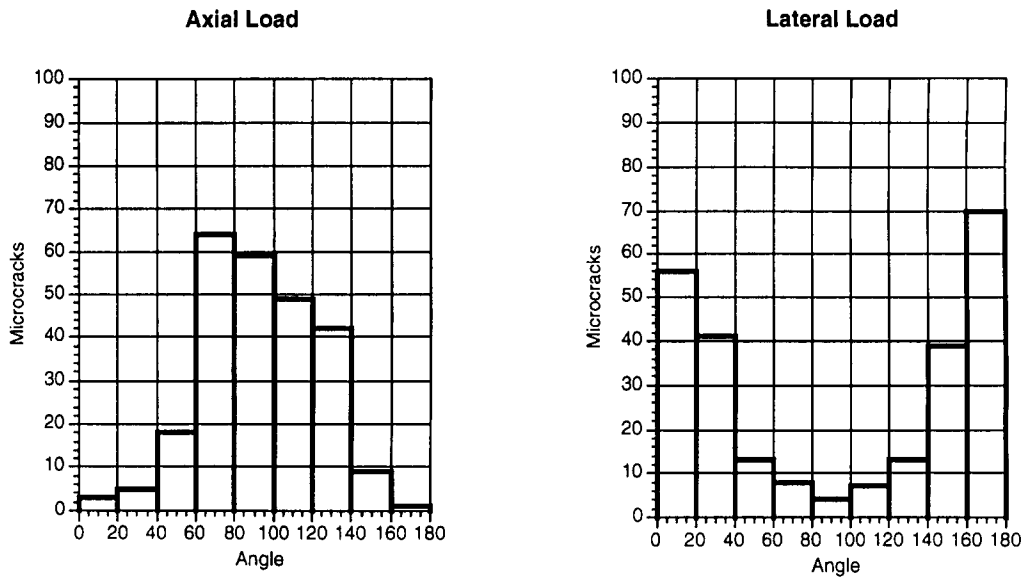

Fig. 16. Microcrack orientation for axial and radial load simulations showing dominant alignment of cracks with load direction (axial direction is 90°).

of intergranular flow channels. For near-hydrostatic loading permeability continues to decrease as the material compacts. At increasing deviatoric stress levels, however, compression-induced permeability reduction is counteracted by enlargement of additional flow channels due to shear and tensile damage to the intergranular bonds and compression-induced intragranular microcracking. The material yields in a dilatant manner. Because the stress-induced microcracks have a preferred orientation parallel to the maximum load direction, permeability of the rock becomes anisotropic at the macroscopic level.

References

Bathurst, R.J. (1985), A study of stress anisotropy in idealized granular assemblies, *Ph.D. Dissertation*, Queen's University at Kingston, Ontario, Canada.

Bathurst, R.J. and L. Rothenburg. (1990), Observations of stress–force–fabric relationships in idealized granular assemblies, *Mech. Mater. 9*, 65–80.

Bernabe Y., D.T. Fryer and J.A. Hayes (1992), The effect of cement on the strength of granular rock, *Geoph. Res. Let. 19 (4)*, 1511–1514.

Bombolakis E.G. (1973), Study of the brittle fracture process under uniaxial compression, *Tectonophysics 18*, 231–248.

Bruno, M.S., C.A. Bovberg and F.M. Nakagawa (1991), Anisotropic stress influence on the permeability of weakly-cemented sandstones, *Proc. of 33rd U.S. Symposium on Rock Mechanics*, Santa Fe, New Mexico, pp. 375–383.

Bruno, M.S. and R.B. Nelson (1991), Microstructural analysis of the inelastic behavior of sedimentary rock, *Mech. Mater. 12*, 95–118.

Chatzis, I. and F.A.L. Dullien (1977), Modelling pore structure by 2-D and 3-D networks with application to sandstones, *J. Can. Pet. Technol. 16*, 97–108.

Christoffersen, J., M.M. Mehrabadi and S. Nemat-Nasser (1981), A micromechanical description of granular material behavior, *J. Appl. Mech. 48*, 339–343.

Cundall, P.A. and O.D.L. Strack (1979), A discrete numerical model for granular assemblies, *Geotechnique 29*, 47–65.

Dobrynin, V.M. (1962), Effect of overburden pressure on some properties of sandstones, *Soc. Pet. Eng. J. 2*, 360–366.

Dullien, F.A.L. (1979), *Porous Media, Fluid Transport and Pore Structure*, Academic Press, New York.

Fatt, I. (1956a), The network model of porous media F. Capillary pressure characteristics, *Trans. AIME 207*, 144–159.

Fatt, I. (1956b), The network model of porous media II. Dynamic properties of a single size tube network, *Trans. AIME 207*, 160–163.

Fatt, I. (1956c), The network model of porous media III. Dynamic properties of networks with tube radius distribution, *Trans. AIME 207*, 164–177.

Fatt, I. and D.H. Davis (1952), Reduction in permeability with overburden pressure, *Pet. Trans., AIME. 195*, 329.

Gallagher J.J., M. Friedman, J. Handin and G.M. Sowers (1974), Experimental studies relating to microfracture in sandstone, *Tectonophysics 21*, 203–247.

Gray, D.H., I. Fatt and G. Bergamini (1963), The effect of stress on the permeability of sandstone cores, *Soc. Pet. Eng. J. 3*, 95–100.

Hallbauer, D.K., H. Wagner and N.G.W. Cook (1973), Some observations concerning the microscopic and mechanical behavior of Quartzite specimens in stiff, triaxial compression tests, *Int. J. Rock Mech. Min. Sci. 10*, 713–726.

Holt, R.M. (1989), Permeability reduction induced by a non-hydrostatic stress field, *Proc. 64th Conf. SPE*, San Antonio, TX, October 8–11, pp. 251–258.

Howard, J.J. (1992), Influence of authigenic-clay minerals on permeability, Origin, Diagenesis, and Petrophysics of Clay Minerals in Sandstones, SEPM special publication No. 47.

Hoshino, K. and H. Koide (1970), Process of deformation of the sedimentary rocks, *Proc. 2nd Congr. Int. Soc. Rock Mech.*, Belgrade, pp. 353–359.

IMSL (1987), *Users Manual, Math / Library, FORTRAN Subroutines for Mathematical Applications*, IMSL, Inc., Houston, TX, p. 167.

Kilmer, N.H., N.R. Morrow and J.K. Pitman (1987), Pressure sensitivity of low permeability sandstones, *J. Pet. Sci. Eng. 1*, 65–81.

Lee, D.H. and C.H. Juang (1988), Use of permeability as an index to characterize internal structural changes and fracture mechanism, *Geotech. Testing J. 11 (1)*, 63–67.

Lockner, D.A., D.E. Moore, and Z. Reches (1992), Microcrack interaction leading to shear fracture, *Proc. of 33rd U.S. Symposium on Rock Mechanics*, Santa Fe, New Mexico, pp. 807–816.

Mavko, G.M. and A. Nur (1978), The effect of nonelliptical cracks on the compressibility of rocks, *J. Geoph. Res. 83*, 4459–4468.

McLatchie, A.S., R.A. Hemstock and J.W. Young (1958), The effective compressibility of reservoir rock and its effects on permeability, *Pet. Trans., AIME 213*, 386–388.

Mehrabadi M.M., S. Nemat-Nasser and M. Oda (1982), On statistical description of stress and fabric in granular materials, *Int. J. Num. Anal. Meth. Geom. 6*, 95–108.

Mordecai, M. and L.H. Morris (1971), An investigation into the changes of permeability occurring in sandstone when failed under triaxial stress conditions, *Proc. of 12th U.S. Symposium on Rock Mechanics*, Rolla, Missouri, pp. 221–238.

Morita, N., K.E. Gray, F.A.A. Srouji and P.N. Jogi (1984), Rock property change during reservoir compaction, SPE Paper 13099, *Proc. 59th Conf. SPE*, Houston, TX, September 16–19.

Oda, M., S. Nemat-Nasser and M.M. Mehrabadi (1982), A statistical study of fabric in a random assembly of spherical granules, *Int. J. Num. Anal. Meth. Geom. 6*, 77–94.

Paterson, M.S. (1978), *Experimental Rock Deformation – The Brittle Field*, Springer, New York, p. 135.

Peng, S.S. and A.M. Johnson (1972), Crack growth and faulting in cylindrical specimens of Chelmsford granite, *Int. J. Rock Mech. Min. Sci. 9*, 37–86.

Plesha, M.E. and E.C. Aifantis (1983), On the modelling of rocks with microstructure, *Proc. of 24th U.S. Symposium on Rock Mechanics*, Texas A&M University, pp. 27–35.

Probine, M.C. (1958), An electrical analogue method of predicting the permeability of unsatured porous media, *B.J. Appl. Phys. 9*, 144–148.

Rhett, D.W. and L.W. Teufel (1992), Stress path dependence of matrix permeability of North Sea sandstone reservoir rock, *Proc. of 33rd U.S. Symposium on Rock Mechanics*, Santa Fe, New Mexico, pp. 345–353.

Rothenburg, L. and R.J. Bathurst, Analytical study of induced anisotropy in idealized granular material, *Geotechnique 39*, 601–614.

Rothenburg, L., E.L. Matyas and S.Z. Ambrus (1987), Statistical aspects of flow in a random network of channels, *Stoch. Hydr. Hydraulics 1(3)*, 217–240.

Sangha, C.M., C.J. Talbot and R.K. Dhir (1974), Microfracturing of a sandstone in uniaxial compression, *Int. J. Rock Mech. Min. Sci. 11*, 107–113.

Seeburger, D.A. and A. Nur (1984), A pore space model for rock permeability and bulk modulus, *J. Geoph. Res. 89 (B1)*, 527–536.

Tapponnier, P. and W.F. Brace (1976), Development of stress-induced microcracks in Westerly granite, *Int. J. Rock Mech. Min. Sci. 13*, 103–112.

Thallak, S., L. Rothenburg and M. Dusseault (1991), Simulation of multiple hydraulic fractures in a discrete element system, *Proc. of 32nd U.S. Symposium on Rock Mechanics*, Norman, Oklahoma, pp. 271–280.

Vairogs, J., C.L. Hearn, D.W. Dareing and V.W. Rhoades (1971), Effect of rock stress on gas production from low-permeability reservoirs, *J. Pet. Tech. 23*, 1161–1167.

Walls, J.D (1982), Tight gas sands – permeability, pore structure, and clay, *J. Pet. Tech. 35*, 2708–2714.

Walsh, J.B. (1965), The effect of cracks on the compressibility of rock, *J. Geophys. Res. 70*, 381–389.

Walsh, J.B. and W.F. Brace (1984), The effect of pressure on porosity and the transport properties of rock, *J. Geoph. Res. 89 (B11)*, 9425–9431.

Wilhelmi, B. and W.H. Somerton (1967), Simultaneous measurement of pore and elastic properties of rocks under triaxial stress conditions, *Soc. Pet. Eng. J. 7*, 283–294.

Yale, D.P. (1984), Network modelling of flow, storage, and deformation in porous rocks, *Ph.D. Dissertation*, Stanford University.

Zhang, J., T.F. Wong, T. Yanagidani and D.M. Davis (1990), Pressure-induced microcracking and grain crushing in Berea and Boise sandstones: acoustic emission and quantitative microscopy measurements, *Mech. Mater. 9*, 1–15.

Zheng, Z., N.G.W. Cook and L.R. Myer (1989), Stress induced microcrack geometry at failure in unconfined and confined axial compressive tests, in: Khair, ed., *Rock Mechanics as a Guide for Efficient Utilization of Natural Resources*, Balkema Press, Rotterdam, pp. 749–756.

Zoback, M.D. and J.D. Byerlee (1976), Effect of high-pressure-deformation on permeability of Ottawa Sand, *AAPG Bul. 60*, 1531–1542.

Zubelwicz, A. and Z.P. Bazant (1987), Interface element modeling of fracture in aggregate composites, *J. Eng. Mech. 113 (11)*, 1619–1630.